

## TOWARD THE DESIGN OF A POSITRON VOLUME IMAGING CAMERA

J.G. Rogers\*, M. Stazyk, R. Harrop\*, C.J. Dykstra\*, J.S. Barney\*, M.S. Atkins\*, and P.E. Kinahan

*TRIUMF, 4004 Wesbrook Mall, Vancouver, B.C., Canada V6T 2A3*Abstract

Three different computing algorithms for performing positron emission image reconstruction have been compared using Monte Carlo phantom simulations. The work was motivated by the recent announcement of the commercial availability of a positron volume imaging camera, the Siemens-CTI 953 B/31[1] which has improved axial (slice) resolution and retractable interslice septa. The simulations demonstrate the importance of developing a complete three-dimensional reconstruction algorithm to deal with the increased gamma detection solid angle and the increased scatter fraction that result when the interslice septa are removed from a ring tomograph. We are developing such an algorithm.

Introduction

The improvements in image quality that will come with the removal of the interslice septa are symmetrical resolution in three dimensions, and increased geometrical sensitivity (which in turn should reduce the statistical noise of the images). The software to utilize the acquired data from a ring tomograph with septa removed must deal with problems not encountered when the septa are in place. Gamma rays will strike the detectors at a much larger range of polar angles. This complicates the image reconstruction problem because the detected gamma rays are no longer organized by the septa to lie in transaxial planes, but rather they sample the object along all lines passing through the cylinder of detectors. The wider acceptance angle also causes an increase in the scatter fraction of the acquired data. If uncorrected by software, this increased scatter causes an additional background noise in the reconstructed images.

The objective of the research described here is to develop an algorithm for three dimensional (3D) image reconstruction which is well suited to the new Siemens-CTI scanner[1], as well as to similar scanners with such "open" geometry, which we expect to see on the market in the future.

The Reconstruction Algorithms Tested

A ring tomograph with interslice septa produces data well suited to slice-by-slice reconstruction with an algorithm originally developed for x-ray CT. The raw form of the data acquired in each slice is the sinogram, which records how many gamma rays were detected at each projection angle and projection distance in the plane of the

slice. 2D reconstruction is the process of filtering and back-projecting, which forms each such 2D sinogram into a 2D image of the part of the object which lies in the plane of the slice. In addition to admitting the detection of events into single-ring "straight slices", septa in multi-ring tomographs are designed so as also to admit gamma-gamma coincidence events with event lines (connecting the two points of detection) which cross from one ring of detectors to an adjacent ring. These cross-plane detections are organized by the acquisition hardware into separate sinograms and reconstructed as if they had originated in an imaginary ring of detectors located midway between the two rings that detected them. This process of reconstructing a three dimensional object as a stack of such straight slices and crossed slices we call "2D reconstruction".

An alternative algorithm proposed for reconstructing images from the new scanner[2] is a modified form of 2D reconstruction[3]. It generalizes the concept of crossed planes, so that all detected events can be used, even those which are detected in rings which are not adjacent. Each event is placed in the slice located midway between the centers of the two rings detecting it. In this algorithm there are no "straight slices" in the sense used above. All slices accumulate events ranging over the full range of polar angles accepted by the 16 rings of detectors which make up the entire scanner. The number of such slices is 31, the same as the total number of straight slices (16) and crossed slices (15) in the 2D reconstruction previously described. We call this the "modified 2D algorithm". It has an advantage over the fully 3D algorithm we are about to describe in that it only requires a minor change in the hardware used to form the sinograms. The image reconstruction software is the conventional 2D algorithm already described.

A new 3D reconstruction algorithm has been developed which is a synthesis of our two earlier algorithms[4,5]. The crucial new feature is the organization of the raw data into a "generalized sinogram", which is formed by incrementing a 4D array of counts. The "generalized sinogram"  $S(p, \xi, \theta, \phi)$  represents the 2D Radon transform[6] of the familiar 4D projection  $P(\ell_x, \ell_y, \theta, \phi)$ [4].

The new algorithm retains the advantage of our second algorithm[5] in that the filtering is accomplished by convolving the "generalized sinogram" with a simple one-dimensional filter function. The filter accomplishes frequency band limiting and second order partial differentiation, as required for Radon transform inversion[5,7]. Because the filter is one-dimensional, computer application of it is fast and has a predictable effect on the statistical

\*also with School of Computing Science, Simon Fraser University, Burnaby, B.C. Canada V5A 1S6

noise of the images. In addition, the new algorithm retains an advantage of our first algorithm[4] in that it performs backprojection along lines through the object, and so should be able to utilize newly developed backprojection hardware[2,7].

The test of the algorithm reported here is simplified in that the objects we chose to reconstruct are limited in their axial extent, so that they are entirely contained in the central few slices. Because of this restriction, the iteration procedure introduced by Rogers, Harrop, and Kinahan[8] is not needed for these tests. However it is directly applicable to the new algorithm and will be required before the algorithm can be applied to real tomograph data (i.e. for sources which extend axially outside the tomograph).

The new algorithm has a disadvantage compared with the 2D and modified 2D algorithms, namely that a more complicated binning procedure than normal is required to form the "generalized sinograms" during scan data acquisition. In previous CTI tomographs sinograms were formed using a hardware device called the realtime sorter[9]. Such a device would have to be designed and built to do the more complicated incrementation needed for "generalized sinograms".

The "generalized sinogram" is a 4D array instead of a set of 2D arrays like normal sinograms. There are thus more choices to be made about what bin sizes should be used in the "generalized sinogram". Because these choices affect the image quality in fundamental ways, we are developing a possible software alternative[10] to the realtime sorter. Especially during the development phase, such software sorting provides ease of changing the binning and binning algorithm to investigate how such changes affect image quality. Inmos transputers[11] offers an attractive choice which we are investigating for implementing a parallel sorting network operating as co-processors to the main reconstruction/display computer.

#### Phantom Simulations of a Small Ellipsoid

The first phantom consisted of an ellipsoid of semi-axis lengths 2 cm (x), 3 cm (y), and 2.5 cm (z). In this and what follows, we take the z-axis along the symmetry axis of the tomograph. The ellipsoid was (simulated to be) uniformly filled with activity except for a number of small spheres (radius=3 mm) which were uniformly filled with activity one-half of the value elsewhere inside the ellipsoid. The detector ring was taken to be a cylinder 102 cm in diameter and 10.6 cm along the z-axis. This ring diameter is the same as that of an earlier CTI tomograph. It was chosen before we knew of the existence of the 953 camera.

In the first simulation, 3.4 million events were simulated and recorded on magnetic tape by a microVAX-II computer. Each event was described by four parameters which specify the event line through the object. In this simulation, detector resolution and object scatter were not included, though they were included in later simulations. The top part of Fig. 1 shows a line drawing of a transaxial section through the ellipsoid. The middle part of the

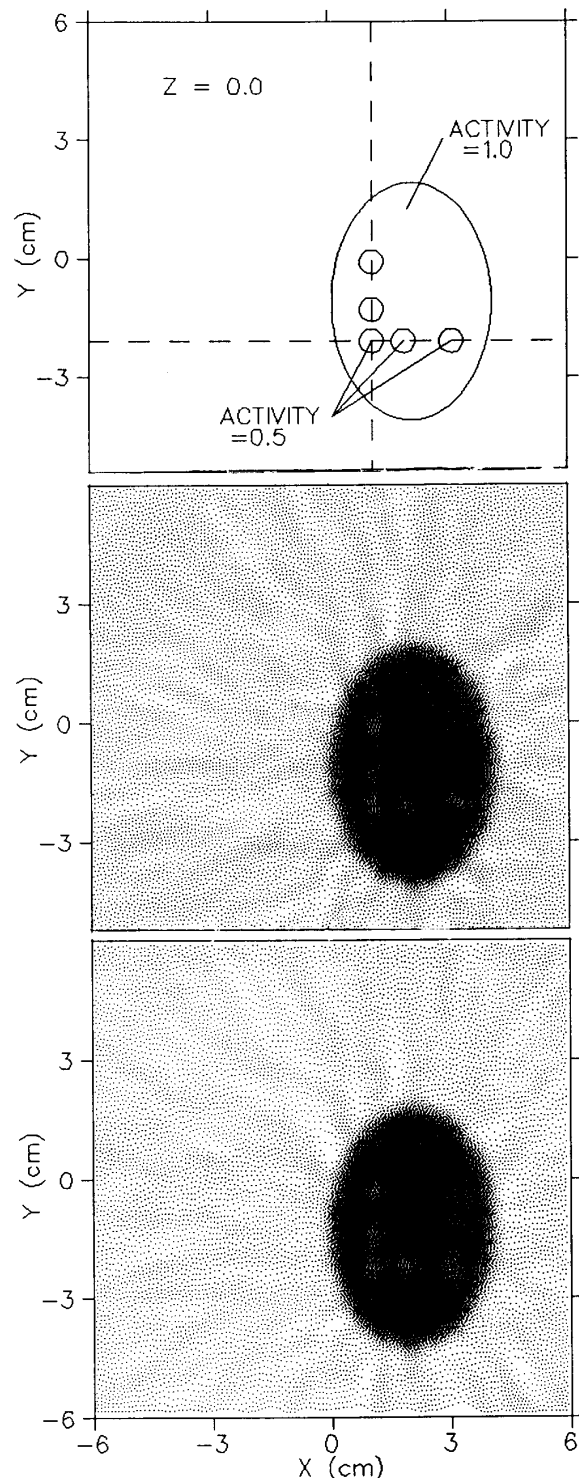


Fig. 1. A transaxial( $z=0$ ) slice of an ellipsoidal phantom. The figure shows: (top) the phantom, (middle) a slice reconstructed with the modified 2D algorithm, and (bottom) the same slice reconstructed with a new 3D algorithm.

figure is a reconstruction using the modified 2D algorithm while the bottom part shows the same transaxial section reconstructed with the new 3D algorithm.

The figure demonstrates that the 3D algorithm has a better noise handling capability than the modified 2D algorithm. Both algorithms incorporate the same number of events, about 90% of the 3.4 million total detections.

Figure 2 shows 1 pixel-wide (=1 mm) sections through the small spheres inside the ellipsoid, taken along the dashed lines in Fig. 1. The sections in the top row were reconstructed with the 2D algorithm, those in the middle row with the modified 2D algorithm, and those in the bottom row with the 3D algorithm. In each of the six panels of Fig. 2 the ideal image section (i.e. the known phantom object) is shown as a straight line drawing overlying the reconstructed image sections.

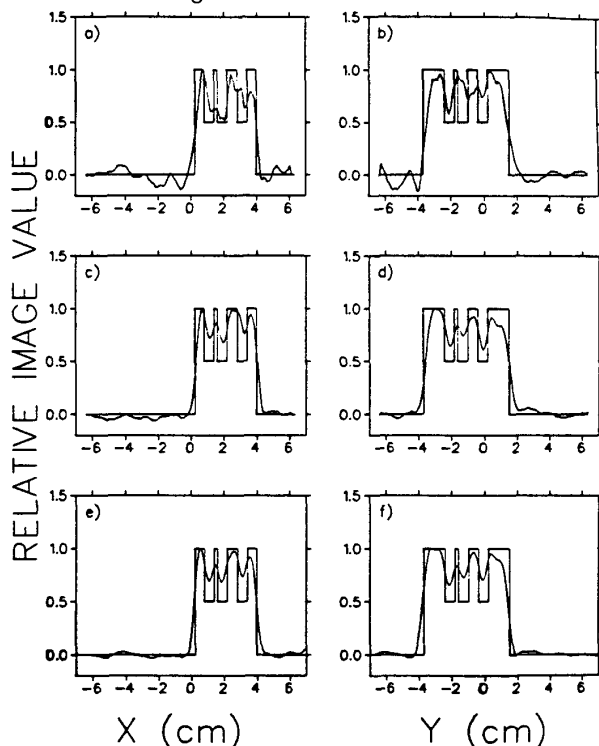


Fig. 2. Line sections of the same ellipsoidal phantom as in Fig. 1, taken along the two dashed lines of Fig. 1. From top to bottom the event data were reconstructed with: (a and b) the conventional 2D algorithm, (c and d) the modified 2D algorithm, and (e and f) a new 3D algorithm. Ideal image sections are shown by straight lines for comparison with the reconstructed sections.

The improvement in image quality between the top row (Figs. 2a and 2b) and the middle row (Figs. 2c and 2d) is due to the incorporation of more events into the sinograms, thereby reducing the statistical noise. The middle images utilize 90% of the detected 3.4 million events, whereas the top images utilize only 12%, the difference being due to the omission from the top images of those

events that would have been absorbed by the septa. Once the septa have been removed, additional improvement in noise can be gained by using the 3D algorithm instead of the modified 2D algorithm.

#### The Effect of Scatter on Volume Images

To investigate the effect of gamma ray scattering in the object being imaged, a second simulation was done with a phantom, consisting of a chest sized elliptical cylinder of water in addition to the ellipsoid containing activity, as shown in Fig. 3a. The scattering cylinder had semi-axes of 15 cm (x) and 11.5 cm (y) and was centered on the axis of the tomograph.

The characterization of scatter done by studying a compact source in an extended scattering medium follows the example of Bergstrom *et al.* in their pioneering work[12] on scatter correction in 2D images. In addition to simplicity of analysis, our choice of phantom made the simulation of detector end shields unnecessary because even if such shields were included, scatter from them would be eliminated by an assumed 450 keV energy threshold. Even with this simplified geometry it took 14 days of CPU time to obtain 1.1 million events on the microVAX computer.

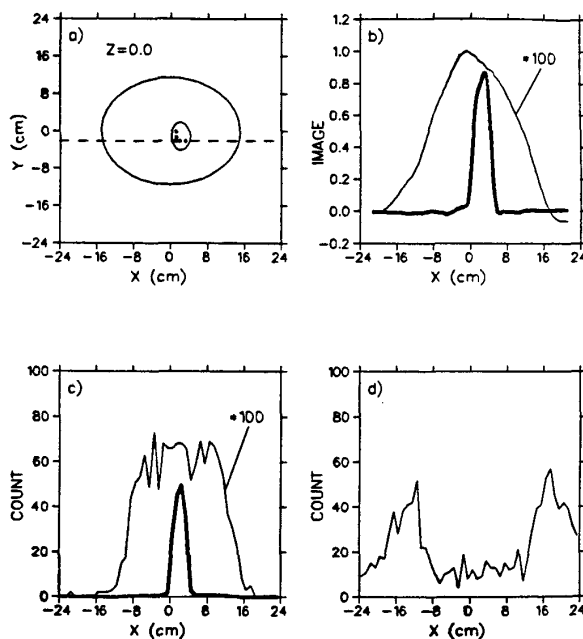


Fig. 3. (a) a transaxial slice of a chest-sized elliptical cylindrical scatterer surrounding the same ellipsoidal phantom of activity as in Fig. 1; (b) reconstructed image sections of the phantom, including all events with both gamma energies above 450 keV (heavy curve), or only scattered events above 450 keV (light curve); (c) sinogram projections at  $\phi=90^\circ$  contributing to the corresponding images of (b); (d) sinogram projection at  $\phi=90^\circ$  of identifiable scattered events with one or both gamma energies in the range 350 - 450 keV.

Figure 3b shows a section of the reconstructed image, along the dashed line of Fig. 3a, obtained by using the modified 2D reconstruction algorithm and a calculated attenuation factor. The heavy curve in Fig. 3b includes all events where both gamma rays reached the detectors with energy above 450 keV. The events in this range which contained scattered gamma rays were reconstructed with a smaller frequency cutoff to smooth out statistical noise. They are plotted as the lighter curve on a 100 times expanded vertical scale. These scattered events are only separable from the unscattered ones in simulation and not in a real measurement because the scattered gamma rays have energies indistinguishable from the full 511 keV annihilation energy, within the resolution of the detectors[1].

Following Bergstrom *et al.*[12] we have studied the scatter contributions to images by examining the projections which contribute to the images. Fig. 3c is an x axis projection, one row of the sinogram, corresponding to the images of Fig. 3b. As expected the scatter has a much wider distribution in the sinogram than do the unscattered events. Figure 3d shows a corresponding projection for events scattered with one or both gamma ray energies in the lower energy range 350-450 keV. These events represent a projection of scattered events that is actually measurable by use of a second energy window in the acquisition hardware. The "low energy scatter" in Fig. 3d is very different in shape from the "high energy scatter" in Fig. 3c, so a simple subtraction of the measured "low energy scatter" to correct for the unmeasurable "high energy scatter" would be a poor correction. Still, with the improved energy resolution ("less than 20%"[1]) of the new block detectors, it seems some use of data acquired in a second energy window to correct for scatter might be possible.

#### Phantom Simulations of an Elliptical Disk

The second phantom chosen for simulation was in the form of a thin elliptical cylinder, as shown in Fig. 4. The phantom was oriented so as to be entirely contained in the "straight" slice defined by one of the two central rings of the CTI 953 B/31 tomograph. The extent of the phantom in the axial direction was one-half the axial sampling

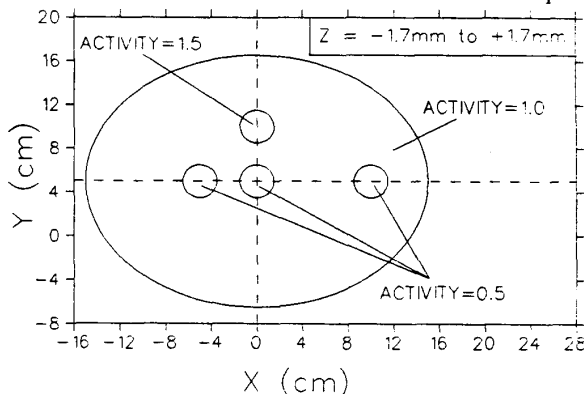


Fig. 4. A transaxial slice of a chest-sized cylindrical disc phantom of activity with one warm and 3 cool cylinders of activity inside.

distance, namely 3.375 mm, whereas in the transverse direction its semi-axes was 15 cm (x) and 11.5 cm (y). The phantom was uniformly filled with activity except inside three circular cylinders where the activity was reduced by 50% and one where the activity was elevated by 50%, compared to the activity elsewhere inside the larger elliptical cylinder.

Figure 5 shows the central slices of three images of the elliptical cylinder reconstructed with the three reconstruction algorithms. As before, the statistical noise improves between the top and middle images, due to the removal of septa, which results in the detection of more events. Of the 4.5 million events produced by the simulation, the top image utilized 10% while the middle and bottom images utilized 80%. The improvement in image quality with the modified 2D algorithm is accompanied by the appearance of an artifact around the edges of the ellipse, especially around the top edge.

This breakdown of the modified 2D algorithm is caused by the spillover of activity from one slice to another due to oblique rays which cross the axial slice boundary inside the field of view[3]. It caused no problem with the previous simulation of a ellipsoid because the object was so small compared to the detector ring.

The 3D algorithm is free of this artifact and also demonstrates a better noise level for the same number of events. This finding confirms the trend we saw previously with the ellipsoidal phantom, but is more significant here because the simulation included some detector resolution effects.

The most important resolution effect included for the first time in the simulations of Fig. 5 (and also included in those to follow in the article) arises from the binning of the gamma detection z-coordinates into discrete detector rings which are separated from each other by 6.75 mm. The effect of this binning is automatically included in the 2D and modified 2D simulations, because both sinograms and image are formed from events grouped into independent slices separated by 3.375 mm. The binning of the z-positions into rings at the detectors has a more subtle effect on the 3D reconstructions. In the simulation, discrete values of ring coordinates (separated by 6.75 mm) were used to compute the polar angle ( $\theta$ ) of each event line, which in turn was used as one of the four indices for incrementing the "generalized sinogram". This z-position binning causes slight ring artifacts which are just visible in the bottom part of Fig. 5 at radii of 10 cm and 20 cm from the tomograph center (which is at  $x=y=0$ ). The simulation is not realistic enough to predict accurately features as small as these. However the future occurrence of such artifacts due to z-position binning in real tomograph data seems likely and needs watching.

Figure 6 shows one-pixel wide (2.5 mm) line sections of the phantom along the two dashed lines in Fig. 4. The artifact in the modified 2D reconstruction shown in the middle row is quite apparent, seen as a depression of the center of the x and y image sections and an elevation on the outsides of the y sections. The 3D image sections (Figs.

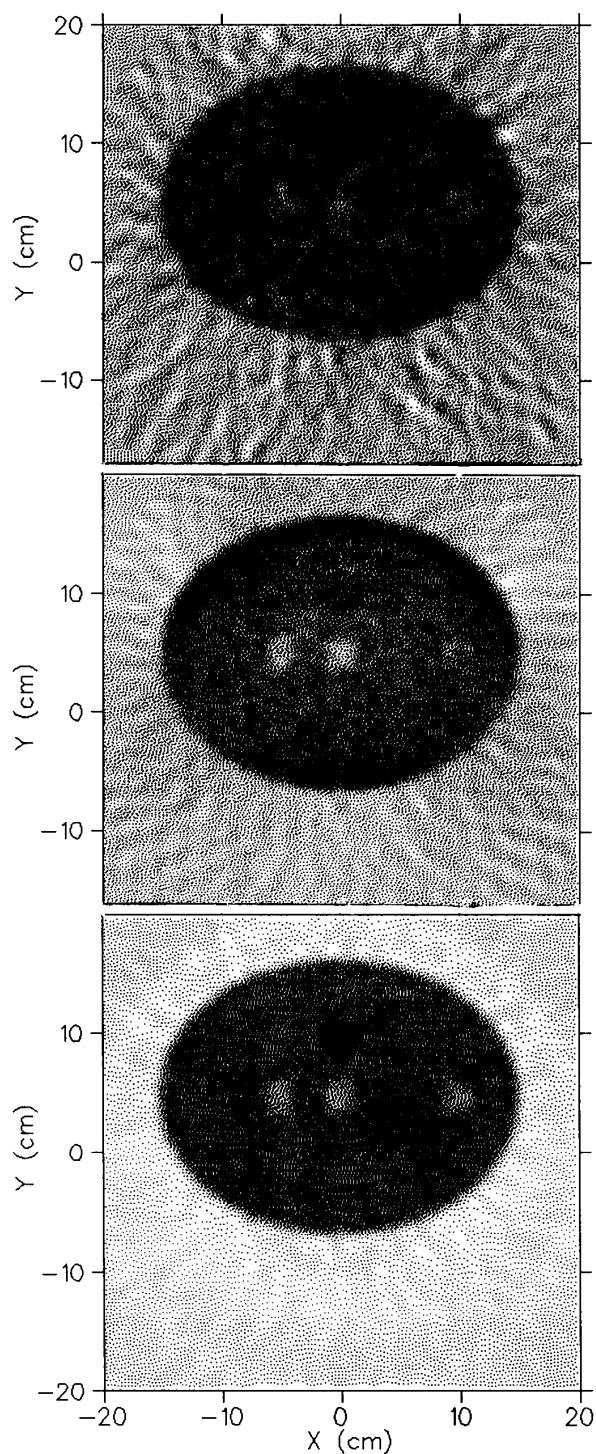


Fig. 5. Transaxial slices reconstructed from the phantom of Fig. 4; (top) using the 2D algorithm, (middle) using the modified 2D algorithm, and (bottom) using a new 3D algorithm.

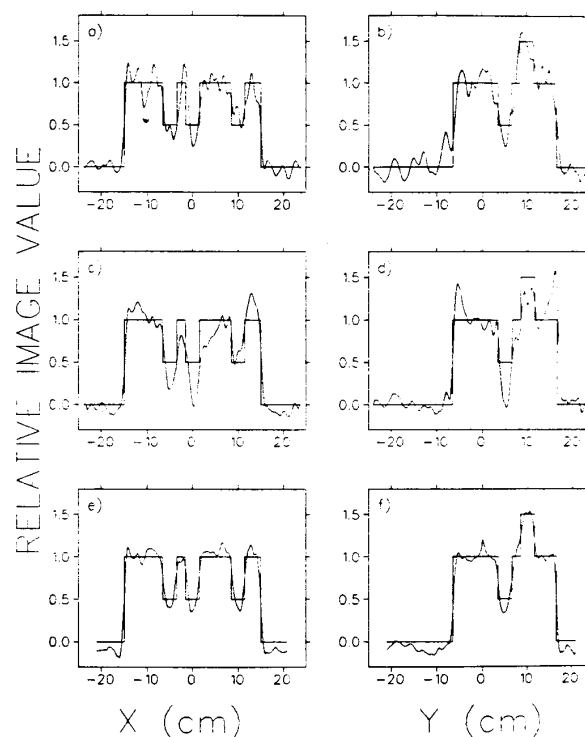


Fig. 6. Line sections reconstructed along the dashed lines of Fig. 4; (a and b) using the 2D algorithms, (c and d) using the modified 2D algorithm and (e and f) using a new 3D reconstruction algorithm. The straight lines show ideal sections of the phantom for comparison with the reconstructed sections.

6e and 6f) are better both in statistical noise and in the absence of artifacts, compared with the modified 2D reconstructions (Figs. 6c and 6d) which incorporate the same number of events.

#### Summary and Conclusions

We have presented a comparison of three different image reconstruction algorithms for positron volume imaging. A new 3D algorithm which is a synthesis of our two earlier algorithms[4,5] seems to have promise for practical use in the new generation of scanners from Siemens-CTI. The 3D algorithm has a lower noise level than either the conventional 2D algorithm (appropriate to tomographs with interslice septa) or the modified 2D algorithm[3] (proposed to implement positron volume imaging on the new scanner)[2]. In addition, the new 3D algorithm is free of a serious artifact that affects the modified 2D algorithm, caused by spillover of activity from one slice to another.

Compared to other 3D algorithms[13,14] the new algorithm seems to have the advantages of employing a very simple one-dimensional filtering operation and of not requiring Fourier transforms. However, to say whether it is better than such algorithms[13,14] will require a comparison of the available 3D algorithms using data from a real positron volume imaging camera.

A brief investigation of the possibility of using a dual energy window to measure scatter confirms earlier studies[15] which show that the spatial distribution of scatter in the image is very sensitive to the final gamma energy.

#### Acknowledgements

Acknowledgement is made of support from the National Science and Engineering Research Council of Canada, the Center for Systems Sciences at Simon Fraser University, and the Science Council of British Columbia. We also thank Cory Kost and Joe Chuma of the TRIUMF Software Services Group for modifying PLOTDATA to make better 2D density plots. We are grateful to Edda Chung of the Tomograph Development Group for preparing most of the figures and to Jana Thomson of the Publications Office for typing the manuscript.

#### References

- [1] Siemens Gammasonics, Inc., 2000 Nuclear Drive, Des Plaines, IL 60018
- [2] Ronald Nutt, CTI PET Systems, Inc., 810 Innovation Drive, Knoxville, TN 37933.
- [3] M.E. Daube-Witherspoon and G. Muehllehner, "Treatment of axial data in three-dimensional PET", *J. Nucl. Med.* **28** 1717 (1987).
- [4] P.E. Kinahan, J.G. Rogers, R. Harrop, and R.R. Johnson, "Three-dimensional image reconstruction in object space", *IEEE Trans.* **NS-35**, 635 (1988).
- [5] C.J. Dykstra, R. Harrop, J.G. Rogers, and P.E. Kinahan, "The Radon transform and positron volume imaging", submitted to *Trans. Med. Imaging* (1989).
- [6] S.R. Deans, "The Radon transform and some of its applications", New York and Toronto, Wiley, 1983, (see chapter 2).
- [7] W.F. Jones, L. Byars, and M. Casey, "Design of a superfast three dimensional projection system for positron emission tomography", *IEEE Trans.* **NS-37** (submitted to this conference).
- [8] J.G. Rogers, R. Harrop, and P.E. Kinahan, "The theory of three-dimensional image reconstruction for PET", *IEEE Trans.* **MI-6** (3), 239 (1987).
- [9] W.F. Jones, M.E. Casey, L. G. Byars and S.G. Burgess, "A VME based real time sorter design for positron emission tomography", *IEEE Trans.* **NS-33**, 601 1986.
- [10] N.A. Wilkinson, M.S. Atkins, and J.G. Rogers, "A tomograph VMEbus parallel processing data acquisition system", *IEEE Trans.*, **NS-36**, 1047 (1989).
- [11] M. Homewood, D. May, D. Shephard and R. Shephard, "The IMS T800 transputer", *IEEE MICRO*, (Oct. 1987), pp 10-26.
- [12] M. Bergstrom, L. Eriksson, C. Bohm, G. Blomqvist and J. Litton, "Corrections for scattered radiation in a ring detector positron camera by integral transformation of the projections", *J. Comput. Assist. Tomogr.* **7**, 42 (1983).
- [13] D.W. Townsend, T. Spinks, T. Jones, A. Geissbuhler, M. Defrise, M.C. Gilardi, and J. Heather, "Three-dimensional reconstruction of PET data from a multi-ring camera", *IEEE Trans.*, **NS-36**, 1056 (1989).
- [14] R. Clack, D. Townsend, and M. Defrise, "An algorithm for 3D reconstruction incorporating cross plane rays", *IEEE Trans.* **MI-8**, 32 (1989).
- [15] M. Dahlbom, L. Eriksson, G. Rosenqvist, and C. Bohm, "A study of the possibility of using multi-slice PET systems for 3D imaging", *IEEE Trans.* **NS-36**, 1066 (1989).